Icarus 209 (2010) 247–255

Contents lists available at ScienceDirect

Icarus

journal homepage: www.elsevier.com/locate/icarus

Accommodation of lithospheric shortening on Mercury from altimetric profiles of ridges and lobate scarps measured during MESSENGER flybys 1 and 2

Maria T. Zuber [a,*], Laurent G.J. Montési [b], Grant T. Farmer [a], Steven A. Hauck II [c], J. Andreas Ritzer [c], Roger J. Phillips [d], Sean C. Solomon [e], David E. Smith [a], Matthieu J. Talpe [a], James W. Head III [f], Gregory A. Neumann [g], Thomas R. Watters [h], Catherine L. Johnson [i]

[a] Department of Earth, Atmospheric and Planetary Sciences, MIT, Cambridge, MA 02139-4307, United States
[b] Department of Geology, University of Maryland, College Park, MD 20742, United States
[c] Department of Geological Sciences, Case Western Reserve University, Cleveland, OH 44106, United States
[d] Planetary Science Directorate, Southwest Research Institute, Boulder, CO 80302, United States
[e] Department of Terrestrial Magnetism, Carnegie Institution of Washington, Washington, DC 20015, United States
[f] Department of Geological Sciences, Brown University, Providence, RI 02912, United States
[g] Solar System Exploration Division, NASA Goddard Space Flight Center, Greenbelt, MD 20771, United States
[h] Center for Earth and Planetary Studies, National Air and Space Museum, Smithsonian Institution, Washington, DC 20560, United States
[i] Department of Earth and Ocean Sciences, University of British Columbia, Vancouver, BC, Canada V6T 1Z4

ARTICLE INFO

Article history:
Received 14 August 2009
Revised 9 January 2010
Accepted 17 February 2010
Available online 27 March 2010

Keywords:
Mercury
Terrestrial planets
Tectonics
Thermal histories

ABSTRACT

The Mercury Laser Altimeter on the NASA MESSENGER mission has ranged to several ridges and lobate scarps during two equatorial flybys of the planet Mercury. The tectonic features sampled, like others documented by spacecraft imaging and Earth-based radar, are spatially isolated and have vertical relief in excess of 1 km. The profiles also indicate that the faulting associated with their formation penetrated to tens of kilometers depth into the lithosphere and accommodated substantial shortening. To gain insight into the mechanism(s) of strain accommodation across these structures, we perform analytical and numerical modeling of representative dynamic localization mechanisms. We find that ductile localization due to shear heating is not favored, given our current understanding of thermal gradients and shallow thermal structure of Mercury at the time of ridge and scarp formation, and is likely to be of secondary importance at best. Brittle localization, associated with loss of resistance during fault development or with velocity weakening during sliding on mature faults, is weakly localizing but permits slip to accumulate over geological time scales. The range of shallow thermal gradients that produce isolated faults rather than distributed fault sets under the assumption of modest fault weakening is consistent with previous models for Mercury's early global thermal history. To be consistent with strain rates predicted from thermal history models and the amount of shortening required to account for the underlying large-offset faults, ridges and scarps on Mercury likely developed over geologically substantial time spans.

1. Introduction

The manner by which a planetary lithosphere experiences contraction and the amount and timing of horizontal shortening provide important information on global thermal history. The style of deformation, brittle or ductile, bears on the thermal and mechanical structure as well as the rate of deformation. As deduced from observed deformation, strain rates coupled with the integrated record of strain provide clues to the processes and rates at which heat is generated and lost from within a planet. Whether deformation takes place in a localized (e.g., along discrete faults) or a spatially distributed (e.g., sets of faults) manner provides pertinent information on lithospheric structure and stress history. In this study we combine altimetric observations (Zuber et al., 2008a,b; Smith et al., 2010) of localized shortening across contractional ridges and lobate scarps on Mercury acquired by the Mercury Laser Altimeter (MLA) (Cavanaugh et al., 2007) on the MErcury Surface, Space ENvironment, GEochemistry, and Ranging (MESSENGER) spacecraft (Solomon et al., 2008; Watters et al., 2009) with analytical and numerical models of localization processes to gain insight into the nature of strain accommodation in the planet's lithosphere.

* Corresponding author. Fax: +1 617 253 7651.
E-mail address: zuber@mit.edu (M.T. Zuber).

0019-1035/$ - see front matter © 2010 Elsevier Inc. All rights reserved.
doi:10.1016/j.icarus.2010.02.026

2. Observations of contractional tectonic features

Images from Mariner 10 (Strom et al., 1975; Melosh and McKinnon, 1988) and MESSENGER (Solomon et al., 2008; Watters et al., 2009) indicate that tectonic structures on Mercury are dominantly contractional in nature. Structural features include lobate scarps, high-relief ridges, and wrinkle ridges, with lobate scarps being the most widespread (Watters et al., 2009). Many of these structures, particularly the lobate scarps, are believed to have formed primarily in response to a decrease in planetary radius (Solomon, 1977; Solomon et al., 2008; Watters et al., 2004, 2009) that accompanied cooling of the interior over the course of the planet's evolution (Solomon, 1977; Hauck et al., 2004; Watters et al., 2004; Zuber et al., 2007). Thermal history models (Solomon, 1976, 1977, 1978, 1979; Schubert et al., 1988; Hauck et al., 2004; Dombard and Hauck, 2008) are generally consistent with the inference from the distribution of lobate scarps and their stratigraphic relations with plains units that contraction initiated prior to the end of heavy bombardment, with the oldest lobate scarps predating smooth plains emplacement and the youngest postdating the most recent plains material (Solomon et al., 2008). Contraction occurred primarily in response to interior cooling associated with the decay of heat-producing elements, but the thermal state and contractional history were also influenced by the extraction of melt from the mantle, the possible cessation of mantle convection, and the nucleation and growth of a solid inner core (Hauck et al., 2004).

The magnitude of accumulated contractional strain provides an important constraint on the thermal history models. Lobate scarp relief has been measured from Mariner 10 stereo-derived topography and Earth-based radar altimetry (Strom et al., 1975; Watters et al., 1998), and from analysis of shadow measurements on MESSENGER images (Watters et al., 2009). Estimates of horizontal shortening across individual scarps inferred from topography and from foreshortened impact craters range from <1 to 3 km (Solomon et al., 2008; Watters et al., 2009). The average areal contractional strain extrapolated globally ranges from 0.06% to 0.08% (Watters et al., 2009).

MESSENGER (Santo et al., 2001; Solomon et al., 2001, 2007) has so far executed three flybys of the planet Mercury, in January and October 2008 and September 2009. During flyby 1, MLA (Cavanaugh et al., 2007) ranged to Mercury's surface and acquired 3617 measurements along a 3200-km-long topographic profile in the equatorial region of the planet (Zuber et al., 2008a; Smith et al., 2010), mostly within the hemisphere of Mercury not imaged by Mariner 10. During flyby 2, MLA acquired 4388 ranges, again along an equatorial profile about 4000 km in length on nearly the opposite hemisphere of the planet, where Mariner 10 and MESSENGER images were available (Zuber et al., 2008b; Smith et al., 2010). No MLA observations were acquired during flyby 3 because a spacecraft safe-hold event halted instrument operations immediately prior to the planned acquisition period for MLA data, although additional images of areas profiled earlier were obtained.

Because MLA ranging to Mercury's surface has so far been restricted to these two flyby profiles, sampling of tectonic features is necessarily limited. Fig. 1 shows five ridges and scarps for which altimetry has been collected, and Table 1 notes locations and measured vertical offsets. For all the lobate scarps measured the offsets exceed 1 km, which is comparable to but at the high end of relief determined for other lobate scarps on Mercury measured from Mariner 10 stereo-derived topography and Earth-based radar altimetry (Watters et al., 1998).

Relief in excess of 1 km is also comparable to the maximum relief of a subset of lobate scarps in the vicinity of the hemispheric dichotomy on Mars (Watters, 2003). However, abundant wrinkle ridges on Hesperian-aged plains of Mars as mapped by the Mars Orbiter Laser Altimeter (Zuber et al., 1992), although similar in cross-sectional shape to the features in Fig. 1, are characterized by surface relief that is less on average by a factor of 3 or more (Golombek et al., 2001).

The most likely explanation for these ridge and scarp structures is that each represents the surface expression of a thrust or reverse fault (Strom et al., 1975; Melosh and McKinnon, 1988; Watters et al., 1998, 2002), perhaps accompanied by multiple splayed minor normal faults near the surface associated with flexural bending of near-surface strata (Plescia and Golombek, 1986; Golombek et al., 2001; Mueller and Golombek, 2004). Secondary structures within ridges and scarps that might be indicative of the complexity of subsurface faulting have not yet been identified in images from the Mariner 10 (Strom et al., 1975; Melosh and McKinnon, 1988) or MESSENGER flybys (Solomon et al., 2008; Watters et al., 2009). But if ultimately revealed by higher-resolution imaging when the MESSENGER spacecraft achieves orbit about Mercury in 2011, back thrusts in association with these structures would indicate mechanical layering of the deformed strata (Cooke and Pollard, 1997; Niño et al., 1998; Schultz, 2000; Okubo and Schultz, 2004). In the current analysis, we focus on interpretation of primary structure, particularly vertical offset. Estimation of strain from a topographic cross-section requires knowledge of the dip of the primary thrust or reverse fault and the penetration of that fault into the lithosphere. Such information is not available for Mercury, and so we limit our analysis to the interpretation of ridge and scarp relief, which is precisely measured by MLA.

Faulting can be either thin- or thick-skinned (Plescia and Golombek, 1986; Watters, 1988), reflecting the depth of fault penetration. On Mars, extensive analysis of the ridges in Lunae Planum indicates thick-skinned deformation, which implies considerable involvement of the lithosphere in faulting and sufficient strength at depth in the lithosphere to maintain conditions appropriate for faulting (Watters, 1991; Zuber, 1995).

As for Mars, the profiles of ridges and scarps on Mercury appear consistent with significant penetration of faulting into the lithosphere. Analysis of the contractional features sampled by stereo imaging (Strom et al., 1975; Watters, 1988) and MLA (Zuber et al., 2008b) indicate that the typical shortening accommodated per feature exceeds that of Martian ridges. Additionally, the areal density of such features on Mercury is considerably lower than on Mars (Watters et al., 2009; Montési and Zuber, 2003a). It appears that contractional deformation on Mercury as manifested by lobate scarps and high-relief ridges is more localized than on Mars. In this analysis we consider the implications of distributed versus localized deformation on Mercury with the intention of gaining insight into the mechanism(s) of strain accommodation.

3. Strain localization

In order to evaluate quantitatively how strain has been accommodated in Mercury's lithosphere, we apply the unified theory of strain localization (Montési and Zuber, 2002). In this formalism, dynamic localization within a planetary material of strength σ occurs via a feedback between rheology and the deformation field. In the most general sense, the rheology relates a set of state variables $\{\chi_i\}$, such as strain, strain rate, strain history, and composition, to the strength of the system through

$$\sigma = \sigma\{\chi_i\}. \tag{1}$$

A special case can be established by defining a parameter χ_o, which we refer to as the localizing quantity (Montési and Zuber, 2002). Dynamic localization of χ_o occurs if the system of internal variables adjusts to a small perturbation of χ_o in such a way that an

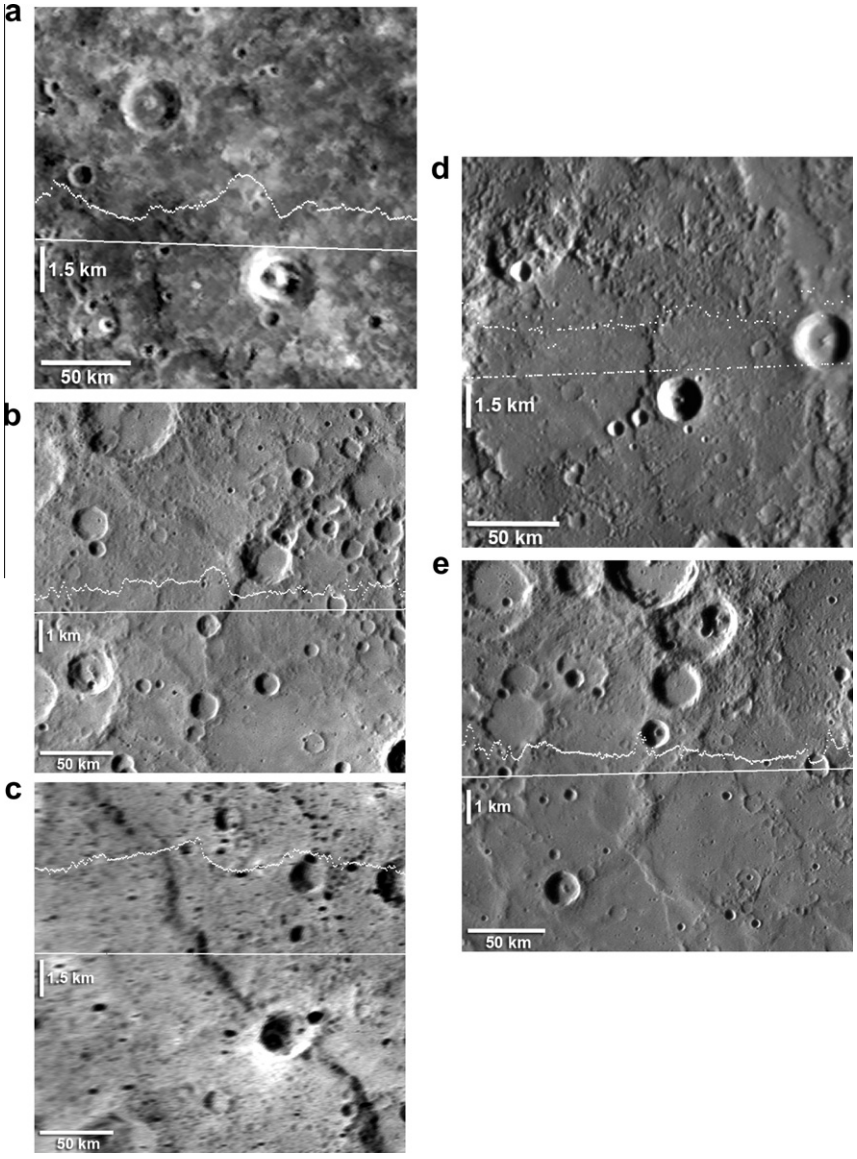

Fig. 1. Topographic profiles of ridges and lobate scarps sampled by the MLA during MESSENGER's first and second flybys of Mercury overlain on images from Mariner 10 and MESSENGER's Mercury Dual Imaging System (MDIS) narrow-angle camera (NAC). The datum for altitude is a sphere of radius 2440 km (Zuber et al., 2008a). Additional details are given in Table 1. Images: (a) Mariner 10 frames 210, 211. (b) MDIS NAC frames EN0108821424M, EN0108821451M. (c) MDIS NAC frame EN0131766454M. (d) MDIS NAC frames EN0131774068M, EN0131774073M. (e) MDIS NAC frames EN0108821424M, EN0108821429M.

Table 1
Tectonic features with MLA topographic profiles from MESSENGER's first and second flybys of Mercury.

Feature type	Lat. (°)	Long. (°E)	Relief (m)
(a) Possible scarp	3.2	−137.6	1430
(b) Lobate scarp	3.5	−104.0	1130
(c) Lobate scarp	4.9	64.7	1420
(d) Possible ridge	2.6	−78.6	1250
(e) Wrinkle ridge	3.3	263.7	680

additional increment of χ_o is generated, which pushes χ_o even farther from its original equilibrium value, i.e., a positive feedback. In particular, if both σ and χ_o are positive, the response of the material that causes localization is a weakening one; the sign of the strength changes is opposite to that of the change of χ_o. The efficiency of localization can be estimated by calculating

$$v_e \equiv \frac{\chi_o}{\sigma}\frac{d\sigma}{d\chi_o}, \tag{2}$$

where v_e is the inverse of the effective stress exponent that describes the relative importance of the dynamic evolution of strength with respect to its current value (Montési and Zuber, 2002). Dynamic localization occurs for negative v_e and is increasingly strong the more negative v_e becomes. We refer to weak localization conditions for which $-0.01 < v_e < 0$. The cutoff value is arbitrary and serves simply to separate cases for which localization may be expected to progress smoothly, corresponding to the tectonic regime, from cases for which a strong runaway is expected, as for impact and adiabatic shear banding in metal forming (e.g., Bai and Dodd, 1992). This formalism is advantageous because of its generality, i.e., it enables a quantitative assessment of the tendency for deformation to localize for many potential mechanisms. Montési and Zuber (2002) derived estimates of the efficiency of localization for a number of localization processes commonly discussed in the literature. The reader is referred to that paper for detailed derivations of the value of v_e for these processes. Here we use that approach to investigate the efficiency of these localization processes on Mercury for the conditions that existed at the time of ridge and scarp forma-

tion. Specifically, we investigate the plausibility of common deformation mechanisms associated with ridges and lobate scarps so far sampled on Mercury (Fig. 1 and Table 1). The plausibility of localization processes provides constraints on the manner by which ridges and lobate scarps on Mercury may have developed.

4. Lithosphere structure

To begin, we construct plausible rheological models for Mercury's lithosphere from compositional and thermal constraints. Reflectance and emission spectra measured from Earth-based telescopes (Vilas, 1988; Sprague et al., 1994, 1997, 2007, 2009) and the geological analysis of color and high-resolution monochrome images obtained from MESSENGER's flybys (Head et al., 2008, 2009a,b; Robinson et al., 2008; Denevi et al., 2009) indicate that a considerable fraction of Mercury's crust had a volcanic origin. A basaltic or diabase composition, with relatively low FeO and substantial plagioclase content, is plausible for the volcanic material, and by extension olivine is likely a major mineral in Mercury's upper mantle (BVSP, 1981). We therefore adopt ductile flow laws for dry Maryland diabase (Mackwell et al., 1998) and dry olivine (Karato et al., 1986; Karato and Wu, 1993) for Mercury's crust and mantle, respectively.

The thermal structure must be estimated for the time of contractional deformation. We assume a surface temperature equal to the average present-day value (Vasavada et al., 1999) and thermal gradients from thermal history models that include convective and conductive cooling and radiogenic heat generation (Hauck et al., 2004). Also relevant are strain rates at the time of ridge and scarp formation, and we assume for bounding purposes the upper limit of current estimates (Nimmo and Watters, 2004; Hauck et al., 2004), 10^{-17} s^{-1}. Similar strain rates are present in large-scale zones of diffuse deformation on Earth, where deformation can be distributed over thousands of kilometers (e.g., Zuber, 1987; Gordon, 2000). Tectonic structures in these diffuse deformation zones often are reactivated faults formed earlier by other processes (Bull and Scrutton, 1990; Delescluse et al., 2008). The absence of equivalent structures, along with the different thermal structure and duration of tectonic episodes, may explain why Mercury's lithosphere has adopted a different tectonic regime than diffuse deformation zones on Earth.

Strength envelopes (Brace and Kohlstedt, 1980) delineating predicted depth ranges of brittle and ductile deformation are given in Fig. 2 for crustal thicknesses of 100 and 50 km (Smith et al., 2010) and for thermal gradients of 8 and 15 K km^{-1}. Adopted lithospheric properties are summarized in Table 2. In the figure, the bilinear segments of the strength profiles represent zones of brittle deformation in which strength is governed by Byerlee's law (Byerlee, 1978), which is independent of rock type. Curved zones of the strength profile represent regions of ductile deformation, which is sensitive to composition, grain size, strain rate, and especially temperature. For comparison, on Earth peak stresses generally occur in the depth range 10–40 km for typical thermal gradients.

For the lower thermal gradient of 8 K km^{-1}, the zone of brittle deformation penetrates to depths of ~38–61 km; for the higher thermal gradient of 15 K km^{-1}, brittle deformation would have been expected to dominate to depths of ~25–30 km. As for Venus, the lack of appreciable crustal water on Mercury results in considerable rock strength, even in light of the high surface temperatures (cf. Mackwell et al., 1998). The low surface gravitational acceleration on Mercury, comparable to that on Mars, also deepens the reach of brittle deformation in comparison with Venus and Earth. The strength of the lithosphere at depths of tens of kilometers is consistent with previous analysis (Nimmo and Watters, 2004) and indicates significant depth penetration of ridge- and scarp-related deformation.

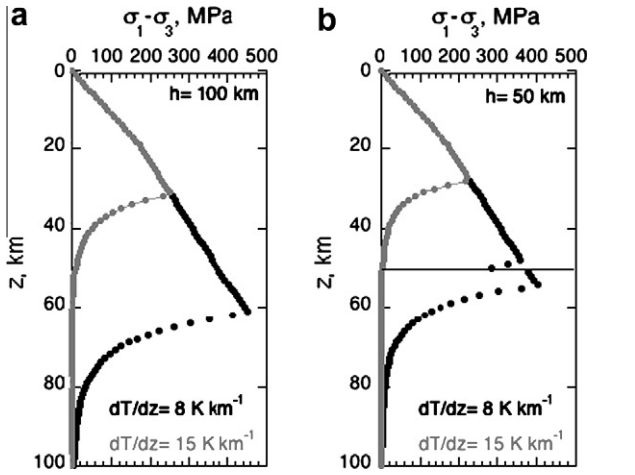

Fig. 2. Lithospheric strength envelopes for Mercury, expressed as the difference between greatest (σ_1) and least (σ_3) compressive principal stress versus depth. (a) 100-km-thick crust, for two different thermal gradients. (b) 50-km-thick crust. The parameters in Table 2 were adopted for the envelopes shown.

Table 2
Adopted properties of the crust and mantle of Mercury.

Strength profile (Fig. 2)
Gravitational acceleration (g) = 3.7 m s^{-2}
Surface temperature (T_o) = 440 K
Thermal gradient (dT/dz) = 8, 15 K km^{-1}
Heat flow = 32, 60 mW m^{-2}
Heat generation (H) = 0.065 mW m^{-3}
Specific heat (C_p) = 1000 J kg^{-1} K^{-1}
Horizontal strain rate ($\dot{\varepsilon}_{xx}$) = 10^{-17} s^{-1}
Crust
Thickness = 50, 100 km
Density = 2900 kg m^{-3}
Flow law for dry Maryland diabase (Mackwell et al., 1998)
n = 4.7
A = 8
Q = 485 kJ mol^{-1}
Mantle
Density = 3300 kg m^{-3}
Flow law for dry olivine (Karato et al., 1986)
n = 3.5
A = 8
Q = 540 kJ mol^{-1}
Brittle failure (Fig. 5)
$\mu_s = \mu_0$ = 0.6
c = 0.003

5. Ductile and brittle localization mechanisms

5.1. Ductile localization – shear heating

Brittle deformation should dominate in the shallow subsurface of Mercury, as indicated in Fig. 2. In the absence of weak mineral phases, which are commonly hydrated, the ductile mechanism that is arguably most likely to contribute to localizing deformation is shear heating, either as a localization mechanism in its own right or for its role in accentuating concurrent strain. Shearing at a horizontal shortening rate $\dot{\varepsilon}_{xx}$ releases energy by viscous dissipation, a fraction β of which is converted into heat H as

$$H = \beta\sigma\dot{\varepsilon}_{xx}, \tag{3}$$

where the lithospheric strength σ in the ductile regime takes the form

$$\sigma = A^{-1/n}\dot{\varepsilon}_{xx}^{1/n}\exp(1/n\theta). \quad (4)$$

In Eq. (4), A and n are material constants, and

$$\theta = TR/Q, \quad (5)$$

where T is absolute temperature, R is the gas constant, and Q is activation energy.

In the absence of a temperature feedback, Eq. (4) implies $v_e = 1/n$. Thus v_e is positive, and so localization is impossible. However, considering that temperature may increase, we may write

$$v_e = \frac{1}{n}\left[1 - \frac{\dot{\varepsilon}_{xx}}{\theta^2}\frac{\partial\theta}{\partial\dot{\varepsilon}_{xx}}\right]. \quad (6)$$

For the case where heat retention is adiabatic over a time t, we may define a heat retention factor

$$T_{ret} = \frac{t}{\rho C_p}, \quad (7)$$

where ρ is density and C_p is heat capacity. The non-dimensional temperature change induced by shearing, or simply heating, $\overline{H}$, is

$$\overline{H} = \frac{T_{ret}HR}{Q}, \quad (8)$$

and allows (6) to be rewritten

$$v_e = \frac{1}{n}\left[1 - \left(1 - \frac{1}{n}\right)\frac{\overline{H}}{\theta^2}\right]. \quad (9)$$

Fig. 3 plots contours of v_e as a function of non-dimensional temperature θ (Eq. (5)) and heating (Eq. (8)). Recalling that the tendency for localization increases for increasingly negative values of v_e, the figure makes clear that localization is favored for high heat generation, i.e., high strain rates and low ambient temperature of the medium. In essence, localization by shear heating requires the heat generation due to ductile creep to exceed the heat content of the medium.

In application to Mercury, Fig. 4 displays v_e as a function of temperature for the dry diabase (Mackwell et al., 1998) and olivine (Karato et al., 1986; Karato and Wu, 1993) rheologies assumed in our lithospheric strength models (Fig. 2 and Table 2). For a strain rate of $10^{-17}\,s^{-1}$, v_e does not become negative unless ambient lithospheric temperatures are considerably lower than inferred for Mercury.

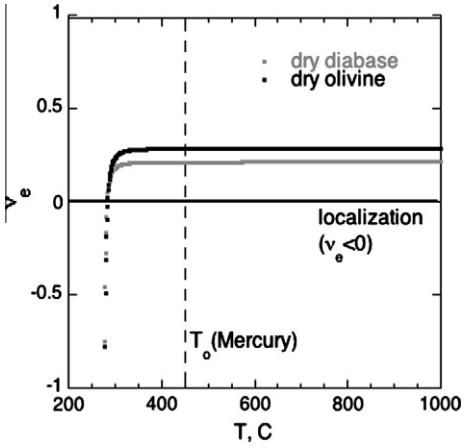

Fig. 4. Plot of v_e versus temperature for the shear heating mechanism with dry diabase (Mackwell et al., 1998) and dry olivine (Karato et al., 1986) rheologies. The shear-zone heating is assumed to be adiabatic.

This evaluation is optimistic in that we assume an upper limit of strain rate as well as adiabatic conditions. In fact, a temperature anomaly will dissipate over a time scale $dt = \rho C_p dx^2/k$, where dx represents the width of the anomaly. If we assume a conservative $dx = 10$ km, at the upper end of the widths of ductile shear zones on Earth (i.e., Vauchez and Tommasi, 2003), a temperature anomaly would dissipate in only 3 Ma, regardless of the anomaly. Thus, there is no point to considering a heat retention time scale of more than a few million years, as heat loss dominates over longer times. Dissipation times are correspondingly shorter for smaller and arguably more reasonable length scales (e.g., $t \sim 30{,}000$ years if $dx = 1$ km), leading to smaller temperature increases. For the thermal parameters in Table 2, a strain rate of $10^{-17}\,s^{-1}$, a stress of 400 MPa, and $t = 3$ Ma, the maximum temperature increase due to shear heating is only 0.12 K.

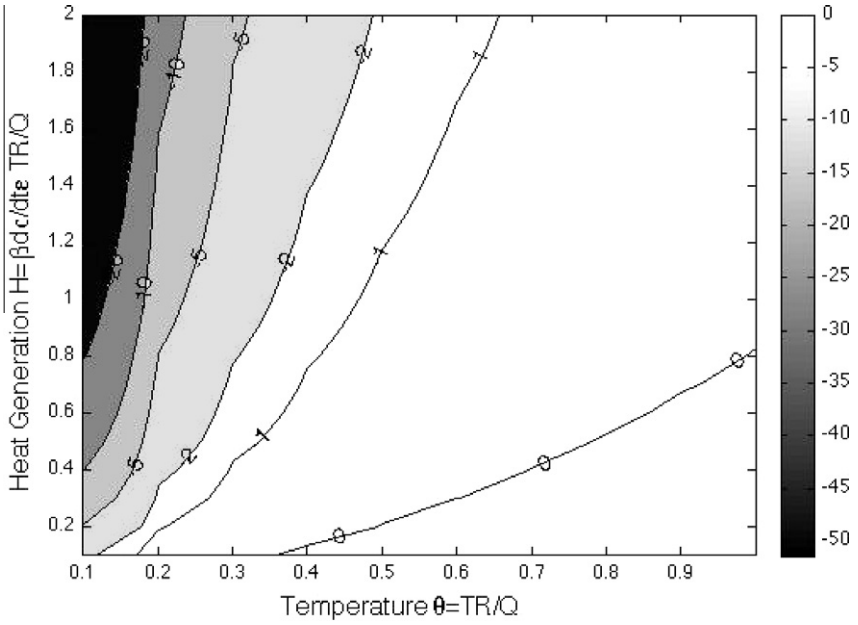

Fig. 3. Tendency for localization due to shear heating as given by the tradeoff of dimensionless heat generation versus the heat content of the medium. Contours are values of v_e. See text for discussion.

Consequently, we conclude that shear heating could not have been a dominant process in ridge and scarp formation, though we do not rule out the possibility that this mechanism operated in local instances where strain rate was significantly greater than global values, such as in the down-dip extension of overlying brittle faults. However, in this case, localization needs to develop in the brittle field before shear heating becomes important.

5.2. Brittle localization – frictional sliding

Deformation in the brittle regime may be envisioned as a volume that deforms by frictional sliding on pervasive faults. Localization occurs when a particular fault or faults accommodates more deformation than others, and it is of interest to contemplate the reason why such a particular fault or faults would do so.

Fault strength is expected to vary with slip during initial stages of fault development, and subsequently with sliding velocity when the fault is mature (e.g., Scholz, 2002). Friction on mature faults is well described by the formalism of the rate- and state-dependent friction regime, which has been characterized from rock mechanics experiments (Dieterich, 1972, 1979; Ruina, 1983). If the long-term strength of faults can be represented by the steady-state sliding relation of Dieterich (1972), mature faults feature a loss of friction with increased sliding velocity given by

$$\mu_d = \mu_0 - c \ln\left(\frac{V}{V_0}\right), \tag{10}$$

where μ_d is dynamic coefficient of friction, appropriate for mature faults, V is slip velocity, the subscript '0' refers to a reference value, and c ($\sim 10^{-2}$) is a constant (Marone, 1998). The static coefficient of friction, μ_s, represents the resistance of inactive faults and is generally higher than μ_d. The transition from static to dynamic friction occurs over a critical distance D_c, estimated at 50 m on Earth (Delescluse et al., 2008).

For the case where friction decreases linearly with sliding distance d we may write (cf. Montési and Zuber, 2002)

$$v_e = \left(1 - \frac{\mu_s}{\mu_s - \mu_d}\frac{D_c}{d}\right)^{-1}, \quad d < D_c. \tag{11}$$

Contours of v_e as a function of normalized slip distance and sliding velocity are plotted in Fig. 5. Localization is weak but favored as the critical distance for the transition from static to dynamic friction is approached. Fig. 6 displays v_e versus μ_d/μ_s for $D_c/d = 1$. The plot shows that there is a linear dependence of localization on friction level. Parameters assumed in this calculation are for steady-state sliding; transient slip could increase the tendency for localization.

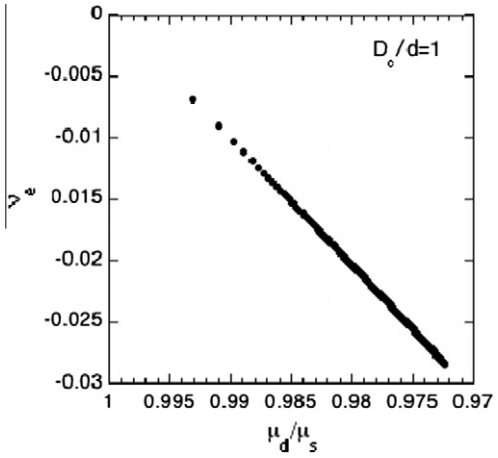

Fig. 6. Plot of v_e versus the ratio of dynamic to static friction, showing increased tendency for localization with friction loss.

The tendency for localization on mature faults, which obey Eq. (10), can be expressed (Montési and Zuber, 2002)

$$v_e = \left[\ln\left(\frac{V}{V_0}\right) - \frac{\mu_0}{c}\right]^{-1}, \quad d > D_c, \tag{12}$$

and indicates that localization is weak, even in the limit of large sliding velocity. The transition from the initial damage regime (Eq. (11)) to the evolved rate-state regime (Eq. (12)) is poorly documented, but the latter is most relevant for large-scale deformation, as fault displacement commonly exceeds D_c. As for Earth, localization is predicted to be weak on Mercury, but if the source of stress is maintained then strain can continue to accumulate. The expectation, supported by thermal models, is that the global contraction of Mercury occurred over geological time scales; during this extended period, intermittent episodes of rapid deformation could have in-

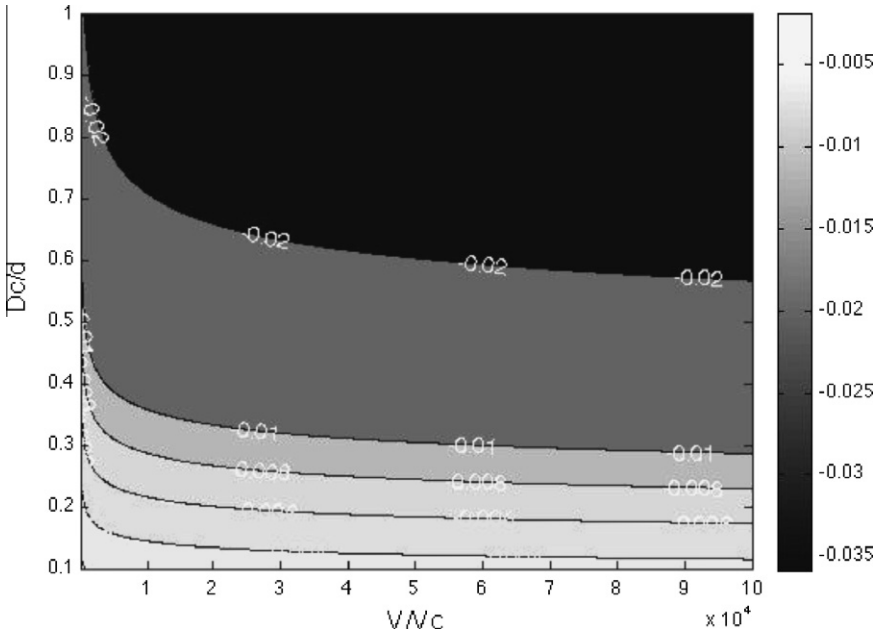

Fig. 5. Contours of v_e for the parameter space of critical slip distance (ordinate) versus critical sliding velocity (abscissa) for a brittle friction loss mechanism.

creased the tendency for localization. The steady accumulation of strain by episodic frictional sliding provides a plausible explanation for large fault offsets if deformation extended over a considerable fraction of Mercury's history.

6. Numerical models of localization

We are interested in understanding the conditions that favor distributed versus localized deformation. More specifically, in keeping with the observations, we wish to identify parameter space(s) that can result in the formation of a single fault that can accommodate considerable strain, rather than a set of closely spaced faults among which shallow strain is distributed.

We begin to address this question with a finite element approach that takes into account localization via a weakening parameter. We utilize the two-dimensional finite element code LAYER (Neumann and Zuber, 1995; Zuber and Parmentier, 1996; Montési and Zuber, 2003a), which solves for the velocity and stress fields of strongly non-Newtonian materials. The effective viscosity of each element is determined at each time step so that the stress is the lowest of a brittle yield envelope and ductile flow law (cf. Fig. 2). Yielding follows the strength of frictional faulting (Byerlee, 1978), modified to account for experimentally observed velocity weakening (Stesky, 1978) associated with stable sliding. In practice dynamic weakening in the brittle regime is simulated by

$$\sigma = (S + fP)[1 - c\,\ln(\dot{\varepsilon}_{xx}/\dot{\varepsilon}_0)], \tag{13}$$

where P is pressure, S and f are experimentally determined constants, $\dot{\varepsilon}_{xx}$ is the horizontal strain rate, and $\dot{\varepsilon}_0$ refers to the reference horizontal strain rate (cf. Neumann and Zuber, 1995). The dependence on strain rate is a continuum representation of velocity weakening on mature faults as in Eq. (10) (Dieterich, 1979; Ruina, 1983). Note that the lithosphere will behave as a continuum if flaws that may be reactivated are more finely spaced than the length scale associated with fault development or spacing, which in turn scales with the thickness of the brittle layer (Montési and Zuber, 2003b). In Eq. (13) the parameter c is the same as in Eq. (10). The tendency for localization (Eq. (2)) associated with Eq. (13) can be expressed (Montési and Zuber, 2003a)

$$v_e = -\frac{c}{1 - c\,\ln(\dot{\varepsilon}_{xx}/\dot{\varepsilon}_0)} \approx -c. \tag{14}$$

This expression, which is analogous in form to Eq. (12), describes localization of the deformation field as implemented in a finite element approach (cf. Montési and Zuber, 2002). Note that in this formulation faults arise spontaneously and need not be included in the finite element calculation *a priori*. In LAYER, horizontal velocities are prescribed along the vertical boundaries of the mesh, tangential velocities are left free at the bottom and sides of the model, and the surface is stress-free. The dimensions of the mesh were chosen in order that details of the prescribed boundary conditions do not affect the character of localization (Farmer et al., 2009). Because the material is incompressible, deformation of the mesh includes shortening accompanied by thickening.

Calculations that result in the localization of horizontal strain rate are shown in Fig. 7 for conditions that result in distributed faults (Fig. 7a), in a single fault (Fig. 7b), or a pair of conjugate faults (Fig. 7c). The figures show $\log(\dot{\varepsilon}_{xx}/\dot{\varepsilon}_0)$ in a lithosphere with a 50-km-thick crust, a weakening factor of 0.2, and other properties as summarized above and in Table 2. Faulting is simulated using Eq. (14), and major spatial concentrations of strain rate correspond to likely zones of faulting. Although these models do not contain the appropriate resolution to capture detailed aspects of shallow deformation (e.g., flexural splays), they have been run to sufficient strains to yield surface relief consistent with ridges on

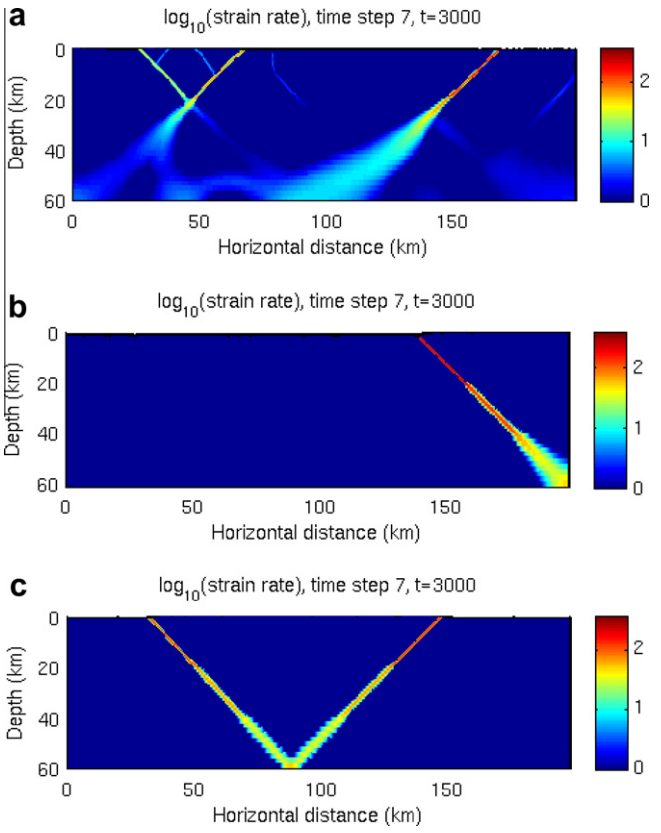

Fig. 7. Finite element solution showing color-coded $\log(\dot{\varepsilon}_{xx}/\dot{\varepsilon}_0)$ for (a) distributed or multiple faults, with dT/dz = 15 K km^{-1}; (b) single-fault case, with dT/dz = 8 K km^{-1}; and (c) two-fault case, with dT/dz = 6 K km^{-1}. These narrow zones of high strain rate represent localization of deformation. For all calculations, the total shortening is 0.6%, the weakening factor is c = 0.2, and the crustal rheology is dry diabase (Mackwell et al., 1998).

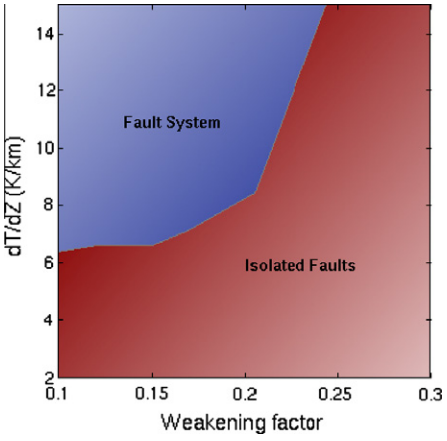

Fig. 8. Results for development of fault systems versus isolated faults (one or two faults; Fig. 7b and c) from finite element analysis. Calculations for all models investigated in the parameter space shown were run for 3000 time steps.

Mercury (Fig. 1, Table 1). In these models fault dip angles are a result of the treatment of plasticity and cannot be used in a predictive sense for tectonic applications.

The only difference between the three runs in Fig. 7 is the assumed thermal gradient. A high thermal gradient (dT/dz = 15 K km^{-1}) yields a system of distributed faults, whereas more modest gradients produce one (dT/dz = 8 K km^{-1}; Fig. 7b) or two (dT/dz = 6 K km^{-1}; Fig. 7c) isolated faults.

The parameter space of thermal gradient and weakening factor is depicted in Fig. 8, which shows the conditions for which a system of faults versus one or two isolated faults develop. The solution space indicates that isolated faults are favored for lower thermal gradients but can occur over the full range of thermal gradients examined (2–15 K km^{-1}) for weakening factors >0.2. For Mercury, low weakening factors are preferred given the weak tendency for brittle localization discussed earlier. Fig. 9 shows thermal gradients at the surface and the base of Mercury's lithosphere in a thermal model by Hauck et al. (2004). The thermal gradients do not exceed 8 K km^{-1} over the planet's evolution, including the early history when ridges and scarps likely nucleated (Solomon et al., 2008). The results presented here are based on solutions for a finite element grid with a spatial dimension of 200 km and a vertical dimension of 60 km. Varying the aspect ratio of the grid slightly changes the boundaries between fields in Fig. 8, but the major feature favoring formation of isolated faults at lower thermal gradients is preserved. These calculations suggest that if frictional weakening operated within Mercury's lithosphere during the planet's early history, then the formation of large, deeply penetrating faults that accommodate significant strain was possible and would be consistent with our understanding of the planet's mechanical structure and thermal state. The fact that ridges are mostly isolated rather than distributed in sets argues that weakening was <0.2 and/or thermal gradients were $\leqslant$8 K km^{-1}, consistent with the thermal models and the estimates of localization efficiency discussed above. By extension, development of a distributed system of faults would have required higher thermal gradients than believed to have been present on the basis of thermal evolution models.

A related question is the specific mechanism of weakening. On the basis of current knowledge of Mercury's lithospheric structure, a detailed assessment of the many conceivable ductile and brittle deformation mechanisms is not warranted. This preliminary assessment shows ductile localization to be very difficult to achieve and brittle mechanisms to be feasible but weak. The fact that ridges and lobate scarps have kilometer-scale vertical offsets indicative of significant lithospheric shortening combined with a weak tendency for localization is consistent with thermal gradients from thermal models and implies accumulation of strain over geologic time.

7. Summary

MESSENGER's Mercury Laser Altimeter (Cavanaugh et al., 2007) has sampled vertical relief on several contractional tectonic features in the equatorial region of Mercury. These features are for the most part isolated spatially and are indicative of substantial localized shortening. While a comprehensive global analysis of the contractional deformation must await altimetric mapping and imaging once MESSENGER enters into orbit about Mercury in March 2011, this study demonstrates the promise for constraining lithosphere structure, and ultimately early thermal state, from the geometry of surface tectonic features. The limited current data set interpreted in the context of rock mechanics information on lithospheric rheology indicates that ridges and scarps penetrate deeply into the lithosphere, consistent with previous work (Nimmo and Watters, 2004). Analysis of representative dynamic localization mechanisms has been applied in an attempt to explain the observations of isolated, large-offset contractional faults. Despite Mercury's high surface temperature, brittle near-surface deformation is favored. Depending on crustal composition and thickness, the zone of expected brittle deformation could penetrate to depths of ~30–60 km. As in the case of Venus (Mackwell et al., 1998), the lack of crustal water on Mercury must be a significant factor in explaining the planet's substantial lithospheric strength.

Localization associated with ridges and scarps on Mercury is best explained by velocity-weakening friction in fault zones. Ductile localization appears to be of secondary importance. Shear heating is favored for high strain rates and low lithospheric heat content and is a possible contributor to downward continuation of brittle faults into the lower lithosphere (tens of kilometers depth) but is unlikely to nucleate faults. Steady-state sliding can accumulate slip over geological time scales and can conceivably explain the observed large-offset faults. The range of thermal gradients that produce isolated faults rather than many distributed faults is consistent with results of global thermal models for Mercury's early history (Hauck et al., 2004).

These preliminary observations indicate that contractional deformation on Mercury has been mostly brittle in nature, is explainable by deep penetration of faults in the lithosphere, and may have operated over a significant span of Mercury's evolution. More detailed observations of tectonic features, their ages, and their relation to the extrusive volcanic history, to be obtained once MESSENGER enters into orbit about Mercury, will serve to elucidate further the dynamics of deformation and its relationship to the planet's thermal evolution.

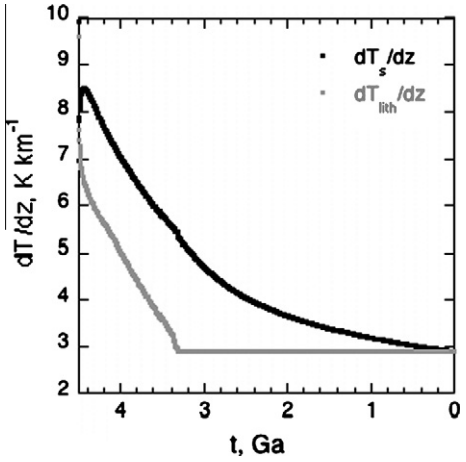

Fig. 9. Thermal gradients at the surface (in black) and the base of the lithosphere (in gray) from a thermal model of Hauck et al. (2004).

Acknowledgments

The MESSENGER project and the Mercury Laser Altimeter investigation are supported by the NASA Discovery Program under Contracts NAS5-97271 to the Johns Hopkins University Applied Physics Laboratory and NASW-00002 to the Carnegie Institution of Washington. We are grateful to Karl Mueller and Stephen Martel for thorough reviews.

References

Bai, Y., Dodd, B., 1992. Adiabatic Shear Localization: Occurrences, Theories, and Applications. Pergamon, New York. 378 pp.
Brace, W.F., Kohlstedt, D.L., 1980. Limits on lithospheric stress imposed by laboratory measurements. J. Geophys. Res. 85, 6248–6252.
Bull, J.M., Scrutton, R.A., 1990. Fault reactivation in the central Indian Ocean and the rheology of oceanic lithosphere. Nature 334, 855–858.
BVSP, 1981. Basaltic Volcanism on the Terrestrial Planets. Pergamon, New York, 1286 pp.
Byerlee, J.D., 1978. Friction of rocks. Pure Appl. Geophys. 116, 615–626.
Cavanaugh, J.F., and 18 colleagues, 2007. The Mercury Laser Altimeter instrument for the MESSENGER mission. Space Sci. Rev. 131, 451–480.
Cooke, M.L., Pollard, D.D., 1997. Bedding-plane slip in initial stages of fault-related folding. J. Struct. Geol. 19, 567–581.
Delescluse, M., Montési, L.G.J., Chamot-Rooke, N., 2008. Fault reactivation and selective abandonment in the oceanic lithosphere. Geophys. Res. Lett. 35, L16312. doi:10.1029/2008GL035066.

Denevi, B.W., and 10 colleagues, 2009. The evolution of Mercury's crust: A newly global perspective from MESSENGER. Science 324, 613–618.
Dieterich, J.H., 1972. Time-dependent friction in rocks. J. Geophys. Res. 77, 3691–3697.
Dieterich, J.H., 1979. Modeling of rock friction, 1. Experimental results and constitutive equations. J. Geophys. Res. 84, 2161–2168.
Dombard, A.J., Hauck II, S.A., 2008. Despinning plus global contraction and the orientation of lobate scarps on Mercury: Predictions for MESSENGER. Icarus 198, 274–276.
Farmer, G.T., Zuber, M.T., Montési, L.G.J., Talpe, M.J., Phillips, R.J., Solomon, S.C., 2009. Characterization of contractional deformation features on Mercury from finite element modeling and altimetric profiles from MESSENGER's flybys. Eos Trans. Am. Geophys. Union (Fall Suppl.) 90 (52). Abstract P21A-1196.
Golombek, M.P., Anderson, F.S., Zuber, M.T., 2001. Martian wrinkle ridge topography: Evidence for subsurface faults from MOLA. J. Geophys. Res. 106, 23811–23821.
Gordon, R.G., 2000. Diffuse oceanic plate boundaries: Strain rates, vertically averaged rheology, and comparisons with narrow plate boundaries and stable interiors. In: Richards, M.A., Gordon, R.G., van der Hilst, R.D. (Eds.), The History and Dynamics of Global Plate Motions, Geophysical Monograph Series, vol. 121. American Geophysical Union, Washington, DC, pp. 143–159.
Hauck II, S.A., Dombard, A.J., Phillips, R.J., Solomon, S.C., 2004. Internal and tectonic evolution of Mercury. Earth Planet. Sci. Lett. 22, 713–728.
Head, J.W., and 10 colleagues, 2008. Volcanism on Mercury: Evidence from the first MESSENGER flyby. Science 321, 69–72.
Head, J.W., and 12 colleagues, 2009a. Volcanism on Mercury: Evidence from the first MESSENGER flyby for extrusive and explosive activity and the volcanic origin of plains. Earth Planet. Sci. Lett. 285, 227–242.
Head, J.W., and 12 colleagues, 2009b. Evidence for intrusive activity on Mercury from the first MESSENGER flyby. Earth Planet. Sci. Lett. 285, 251–262.
Karato, S.-I., Wu, P., 1993. Rheology of the upper mantle: A synthesis. Science 260, 771–778.
Karato, S.-I., Paterson, M.S., FitzGerald, K.D., 1986. Rheology of synthetic olivine aggregates: Influence of grain size and water. J. Geophys. Res. 91, 8151–8176.
Mackwell, S.J., Zimmerman, M.E., Kohlstedt, D.L., 1998. High-temperature deformation of dry diabase with application to tectonics on Venus. J. Geophys. Res. 103, 975–984.
Marone, C., 1998. Laboratory-driven friction laws and their applications to seismic faulting. Ann. Rev. Earth Planet. Sci. 36, 643–696.
Melosh, H.J., McKinnon, W.B., 1988. The tectonics of Mercury. In: Vilas, F., Chapman, C.R., Matthews, M.S. (Eds.), Mercury. University of Arizona Press, Tucson, pp. 374–400.
Montési, L.G.J., Zuber, M.T., 2002. A unified description of localization for application to large-scale tectonics. J. Geophys. Res. 107, 2045. doi:10.1029/2001JB000465.
Montési, L.G.J., Zuber, M.T., 2003a. Clues to the lithospheric structure of Mars from wrinkle ridge sets and localization instability. J. Geophys. Res. 108, 5048. doi:10.1029/2002JE001974.
Montési, L.G.J., Zuber, M.T., 2003b. Spacing of faults at the scale of the lithosphere and localization instability: 1. Theory. J. Geophys. Res. 108, 2110. doi:10.1029/2002JB001923.
Mueller, K., Golombek, M.P., 2004. Compressional structures on Mars. Ann. Rev. Earth Planet. Sci. 43, 435–464.
Neumann, G.A., Zuber, M.T., 1995. A continuum approach to the development of normal faults. In: Daemen, J.J.K., Schultz, R.A. (Eds.), Proceedings of the 35th U.S. Symposium on Rock Mechanics. Balkema, Lake Tahoe, Nev., pp. 191–198.
Nimmo, F., Watters, T.R., 2004. Depth of faulting on Mercury: Implications for heat flux and effective elastic thickness. Geophys. Res. Lett. 31, L02701. doi:10.1029/2003GL018847.
Niño, F., Philip, H., Chéry, J., 1998. The role of bed-parallel slip in the formation of blind thrust faults. J. Struct. Geol. 20, 503–516.
Okubo, C.H., Schultz, R.A., 2004. Mechanical stratigraphy in the western equatorial region of Mars based on thrust fault-related fold topography and implications for near-surface volatile reservoirs. Geol. Soc. Am. Bull. 116, 584–605.
Plescia, J.B., Golombek, M.P., 1986. Origin of planetary wrinkle ridges based on the study of terrestrial analogs. Geol. Soc. Am. Bull. 97, 1289–1299.
Robinson, M.S., and 12 colleagues, 2008. Reflectance and color variations on Mercury: Regolith processes and compositional heterogeneity. Science 321, 66–69.
Ruina, A.L., 1983. Slip instability and state variable friction laws. J. Geophys. Res. 88, 10359–10370.
Santo, A.G., and 25 colleagues, 2001. The MESSENGER mission to Mercury: Spacecraft and mission design. Planet. Space Sci. 49, 1481–1500.
Scholz, C.H., 2002. The Mechanics of Earthquakes and Faulting, second ed. Cambridge University Press. 496 pp.
Schubert, G., Ross, M.N., Stevenson, D.J., Spohn, T., 1988. Mercury's thermal history and the generation of its magnetic field. In: Vilas, F., Chapman, C.R., Matthews, M.S. (Eds.), Mercury. University of Arizona Press, Tucson, pp. 429–460.
Schultz, R.A., 2000. Localization of bedding plane slip and backthrust faults above blind thrust faults: Keys to wrinkle ridge structure. J. Geophys. Res. 105, 12035–12052.
Smith, D.E., and 11 colleagues, 2010. The equatorial shape and gravity field of Mercury from MESSENGER flybys 1 and 2. Icarus, 209, 88–100.
Solomon, S.C., 1976. Some aspects of core formation in Mercury. Icarus 28, 509–521.
Solomon, S.C., 1977. The relationship between crustal tectonics and internal evolution in the Moon and Mercury. Phys. Earth Planet. Interiors 15, 135–145.
Solomon, S.C., 1978. On volcanism and thermal tectonics on one-plate planets. Geophys. Res. Lett. 5, 461–464.
Solomon, S.C., 1979. Formation, history and energetics of cores in the terrestrial planets. Phys. Earth Planet. Interiors 19, 168–182.
Solomon, S.C., and 20 colleagues, 2001. The MESSENGER mission to Mercury: Scientific objectives and implementation. Planet. Space Sci. 49, 1445–1465.
Solomon, S.C., McNutt Jr., R.L., Gold, R.E., Domingue, D.L., 2007. MESSENGER mission overview. Space Sci. Rev. 131, 3–39.
Solomon, S.C., and 10 colleagues, 2008. Return to Mercury: A global perspective on MESSENGER's first Mercury flyby. Science 321, 59–62.
Sprague, A.L., Kozlowski, R.W.H., Witteborn, F.C., Cruikshank, D.P., Wooden, D.H., 1994. Mercury: Evidence for anorthosite and basalt from mid-infrared (7.3–13.5 micron) spectroscopy. Icarus 109, 156–167.
Sprague, A., Nash, D.B., Witteborn, F.C., Cruikshank, D.P., 1997. Mercury's feldspar connection, mid-IR measurements suggest plagioclase. Adv. Space Res. 19, 1507–1510.
Sprague, A., Warrell, J., Cremonese, G., Langevin, Y., Hilbert, J., Wurz, P., Veselovsky, I., Orsini, S., Milillo, A., 2007. Mercury's surface composition and character as measured by ground-based observations. Space Sci. Rev. 131, 399–431.
Sprague, A.L., Donaldson Hanna, K.L., Kozlowski, R.W.H., Helbert, J., Maturilli, A., Warell, J.B., Hora, J.L., 2009. Spectral emissivity measurements of Mercury's surface indicate Mg- and Ca-rich mineralogy, K-spar, Na-rich plagioclase, rutile, with possible perovskite and garnet. Planet. Space Sci. 57, 364–383.
Stesky, R., 1978. Mechanisms of high temperature frictional sliding in Westerly granite. Can. J. Earth Sci. 15, 361–375.
Strom, R.G., Trask, N.J., Guest, J.E., 1975. Tectonism and volcanism on Mercury. J. Geophys. Res. 80, 2478–2507.
Vasavada, A.R., Paige, D.A., Wood, S.E., 1999. Near-surface temperatures on Mercury and the Moon and the stability of polar ice deposits. Icarus 141, 179–193.
Vauchez, A., Tommasi, A., 2003. Wrench faults down to the asthenosphere: Geological and geophysical evidence and thermomechanical effects. In: Storti, F., Holdsworth, R.E., Salvini, F. (Eds.), Intraplate Strike-Slip Deformation Belts, vol. 210. Geological Society London, Special Publication, pp. 15–34.
Vilas, F., 1988. Surface composition of Mercury from reflectance spectrophotometry. In: Vilas, F., Chapman, C.R., Matthews, M.S. (Eds.), Mercury. University of Arizona Press, Tucson, pp. 59–76.
Watters, T.R., 1988. Wrinkle ridge assemblages on the terrestrial planets. J. Geophys. Res. 93, 10236–10254.
Watters, T.R., 1991. Origin of periodically spaced wrinkle ridges on the Tharsis plateau of Mars. J. Geophys. Res. 96, 15599–15616.
Watters, T.R., 2003. Thrust faults along the dichotomy boundary in the eastern hemisphere of Mars. J. Geophys. Res. 108, 5054. doi:10.1029/2002JE001934.
Watters, T.R., Robinson, M.S., Cook, A.C., 1998. Topography of lobate scarps on Mercury: New constraints on the planet's contraction. Geology 26, 991–994.
Watters, T.R., Schultz, R.A., Robinson, M.S., Cook, A.C., 2002. The mechanical and thermal structure of Mercury's early crust. Geophys. Res. Lett. 29, 1542. doi:10.1029/2001GL014308.
Watters, T.R., Robinson, M.S., Bina, C.R., Spudis, P.D., 2004. Thrust faults and the global contraction of Mercury. Geophys. Res. Lett. 31, L04701. doi:10.1029/2003GL019171.
Watters, T.R., Solomon, S.C., Robinson, M.S., Head, J.W., Andre, S.L., Hauck II, S.A., Murchie, S.L., 2009. The tectonics of Mercury: The view after MESSENGER's first flyby. Earth Planet. Sci. Lett. 285, 283–296.
Zuber, M.T., 1987. Compression of oceanic lithosphere: An analysis of intraplate deformation in the Central Indian Basin. J. Geophys. Res. 92, 4817–4825.
Zuber, M.T., 1995. Wrinkle ridges, reverse faulting, and the depth penetration of lithospheric strain in Lunae Planum, Mars. Icarus 114, 80–92.
Zuber, M.T., Parmentier, E.M., 1996. Finite amplitude folding of a continuously viscosity-stratified lithosphere. J. Geophys. Res. 101, 5489–5498.
Zuber, M.T., Smith, D.E., Solomon, S.C., Muhleman, D.O., Head, J.W., Garvin, J.B., Abshire, J.B., Bufton, J.L., 1992. The Mars Observer Laser Altimeter investigation. J. Geophys. Res. 97, 7781–7797.
Zuber, M.T., and 11 colleagues, 2007. The geophysics of Mercury: Current status and anticipated insights from the MESSENGER mission. Space Sci. Rev. 131, 105–132.
Zuber, M.T., and 13 colleagues, 2008a. Laser altimeter observations from MESSENGER's first Mercury flyby. Science 321, 77–79.
Zuber, M.T., and 13 colleagues, 2008b. Topography of equatorial Mercury from MESSENGER flybys 1 and 2. Eos Trans. Am. Geophys. Union (Fall Suppl.), 89 (53). Abstract U11C-04.